Interdisciplinary Sciences: Computational Life Sciences manuscript No.
(will be inserted by the editor)

Tracking the Progression & Influence of Beta-Amyloid Plaques Using Percolation Centrality and Collective Influence Algorithm: A Study using PET images

Gautam Kumar Baboo · **Raghav Prasad** ·
Pranav Mahajan · **Veeky Baths**

Received: date / Accepted: date

Abstract Purpose:Network analysis allows investigators to explore the many facets of brain networks, particularly the proliferation of disease. One of the hypotheses behind the disruption in brain networks in Alzheimer's disease (AD) is the abnormal accumulation of beta-amyloid plaques and tau protein tangles. In this study, the potential use of percolation centrality to study beta-amyloid movement studied as a feature of given PET image-based networks.
Methods: The PET image-based network construction is possible using a public access database - Alzheimer's Disease Neuroimaging Initiative, which provided 551 scans. For each image, the Julich atlas provides 121 regions of interest, which are the network nodes. Besides, the influential nodes for each scan are calculated using the collective influence algorithm.
Results:Analysis of variance ($p<0.05$) yields the region of interest Gray Matter Broca's Area for PiB tracer type for all nodal metrics, whereas, for AV45, the Gray Matter Hippocampus region is significant for three of the metrics. Pairwise variance analysis between the clinical groups yields five and twelve statistically significant ROIs for AV45 and PiB, capable of distinguishing between pairs of clinical conditions. Multivariate linear regression between the percolation centrality values for nodes and

F. Author
Cognitive Neuroscience Lab, Department of Biological Sciences
Tel.: +91 78755 16714
ORCID: 0000 0003 1072 4144
E-mail: p20130404@goa.bits-pilani.ac.in

S. Author
Cognitive Neuroscience Lab, Department of Biological Sciences
E-mail: f20170297@goa.bits-pilani.ac.in

T. Author Cognitive Neuroscience Lab, Department of Biological Sciences
E-mail: f20170277@goa.bits-pilani.ac.in
· Corresponding Author (C. Author)
Cognitive Neuroscience Lab, Department of Biological Sciences
Tel.: +91 832 2580 436
E-mail: veeky@goa.bits-pilani.ac.in

psychometric assessment scores reveals Mini-Mental State Examination is a reliable metric. Finally, a ranking of the regions of interest is based on the collective influence algorithm to indicate the anatomical areas strongly influencing the beta-amyloid network.
Conclusion:This study demonstrates that percolation centrality values indicate the regions of interest that reflect the disease's spread. .

Keywords PET · Alzheimer's Disease · Graph Theory · Percolation Centrality · Collective influence

1 Introduction

Alzheimer's disease predominantly stands out when it comes to neurodegenerative diseases—affecting the middle-age (early-onset Alzheimer's disease (AD)) and the old-age (Late-onset AD) human population. Current projections are estimated to cost about 2 trillion US Dollars by 2030[15], affecting 75 million individuals by the same year. The indirect costs are estimated to be about 244 billion US Dollars[1]. With no sight of a cure for AD and with increasing cases, early diagnosis and active management are the keys to tackling this disease for now. The ability to predict the disease's progression with high accuracy helps design a suitable treatment regime at an early stage, thereby bringing the disease's management to an affordable cost range.

The current methods of diagnosis of the disease include both non-invasive and invasive techniques of investigations ranging from Positron Emission Tomography (PET) scans or Cerebrospinal Fluid (CSF) analysis to bedside pen and paper-based questionnaires; each with its pros and cons.
The ability to accurately determine that dementia is due to Alzheimer's is of utmost importance, followed by the ability to indicate the severity of the disease, which is a unique challenge.

A combination of techniques or criteria is currently employed to detect and determine the extent of dementia due to AD. Methods which include family history, psychiatric history for cognitive and behavioral changes, which is then followed by psychometric assessments such as Mini-Mental State Examination (MMSE) [56], Frontal Assessment Battery[13], and the Neuropsychiatric Inventory Questionnaire (NPIQ)[6].
Others include Genetic testing[31] for markers of AD, the apolipoprotein-e4 (APOE-e4)[20], or the use of blood testing or brain imaging to rule out dementia due to other factors. The use of PET imaging[24] and lumbar puncture[49] to determine the levels of beta amyloids in either of them beyond the normal levels is the current standard of practice for the determination of dementia due to AD[34, 51].

Positron Emission Tomography or PET imaging involves the use of radiopharmaceuticals such as 2-[18F], florbetapir-fluorine-18 (AV45), or 11C-Pittsburgh compound B (PiB). AV45 and PiB[30] are comparatively newer and different in terms of the image construction mechanism. Both AV45 and PiB bind to beta-amyloid but vary in their half-life. AV45 has a half-life of 109.75 minutes and PiB, 20 minutes[62]. A comparison between PiB and AV45 varies because AV45 shows uptake within the white matter regions[53].

The application of network analysis/graph theory to anatomical neural networks has proved helpful in understanding brain connectivity[43, 52] deviations under various psychological and neurological disease states. Network analysis on neuroimaging data such as EEG, MEG, fMRI, and PET scans proves to be helpful to show the variation between a cognitively normal population versus other diagnostic states using various graph-theoretic metrics[46, 57].

Graph metrics such as characteristic path length, clustering coefficient, modularity, and hubs have been studied and have provided insights into the brain networks of AD patients and control groups. Some studies have tried to map the progression of MCI to dementia due to AD [7, 55]; thus, network analysis and the various graph metrics have shown potential as a tool to investigate the brain networks. Network analysis on AD is a practical application wherein it describes the Alzheimer's brain network's behavior. Connectivity analysis using fMRI and EEG data reports provides mixed responses; when comparing AD patients and the control group[55], there is an increase or decrease in the network's connectivity. A reduction in connectivity could explain the cortical atrophy/disruption of the network. An increase could explain the compensatory mechanism[61].

Network Analysis on PET images related to AD mainly revolve around learning models or are limited to tracers that focus on the metabolic networks and the associated deviations of these networks[5, 50]. Other methods include applying algorithms to the raw PET images to recognize patterns to resolve differences between healthy controls and patients with neurodegeneration[27]. Recent methods include genetic and protein markers to improve predicting the course of the disease[17]. These methods rely on many data points and equally reliable computing hardware; this is currently a challenge. Given that AD diagnosis is a global challenge, a method that works well in a spectrum of nations, from developed countries such as the United States to rural hospitals of southeast Asia or Africa[1] is necessary. Methods such as principal component analysis have a few drawbacks; for instance, choosing the number of principal components and data standardization for multiple PET scans of patients with different tracers leads to controlling multiple variables. Regression analysis is based on the assumption that there are cause and effect in place. Furthermore, a relationship that is present within a limited data set might get overturned with a detailed data set.

To understand beta-amyloid propagation, we propose applying graph theoretic methods on PET images to understand beta-amyloid advancement. The main benefit of adding this method is that

1. This does not introduce any new steps for data collection from the patient and, at the same time
2. adds value to the existing data by computing the percolation centrality of a given node at a given time

Network topology offers insights into the evolution of the network in a clinical setting. Studying such an evolution provides a possibility to understand the weak links within atlas based region of interest(ROI) networks. Such networks' structural connectivity information might yield the source and sink of neurodegeneration with the brain architecture.

Percolation centrality is defined as the proportion of 'percolated paths' that pass through that node; this measure quantifies the relative impact of nodes based on their topological connectivity, as well as their percolated states. In other words, it is one such graph metric that looks at the extent to which a given node within a network has percolated information or can percolate information(see figure 2.). The volume of information transmitted via a given node is provided by values ranging from 0.0 to 1.0[38, 42]. Prior exploration of percolation centrality on disease networks[35, 39, 42, 48] and percolation centrality in disease networks of the brain[8] have shown this as a promising metric for brain network investigation.

The knowledge on the application of percolation centrality on human PET-image-based networks is scarce at present. This work aims at adding knowledge to the gap. On the other hand, collective influence provides a minimum set of nodes or regions of the interest that can transfer information or spread disease with ease with optimal spread[37] based on the optimal percolation theory. By examining the network for the minimum set of nodes, this set will provide the regions of interest within the brain that optimally move beta-amyloid, disrupting the normal functioning of the existing neural networks.

Thus, the ability to detect the disease and predict the rate of progression of the disease at an early stage is imperative. To this end, the study aims to answer two main questions: 1) Can percolation centrality measure be used to determine the percolation of beta-amyloids within the brain? 2) Can the collective influence algorithm provide a minimum set of nodes that are vital to the AD network?

2 Materials and Methods

2.1 Current Ethics Statement

2.1.1 IRB Waiver Statement

Informed consent from the patients is obtained before the assessment carried out by the ADNI study team (See ADNI website for details), and this study is a secondary data analysis of the ADNI data collection, which aims at providing a simplified metric to an already diagnosed patient. The data access and usage is within the ADNI data use agreements.

2.1.2 Patient Distribution

Based on the tracer agents used for acquiring the PET images, each diagnostic state subset of the data set is divided into the two available tracers; AV45[4] and PiB[62]. The patients are categorized as Cognitively normal, with Mild Cognitive Impairment, or having Alzheimer's Disease (AD) based on the ADNI study's psychometric assessments. Next, the PET image is matched with the patient's diagnostic state at the time of the imaging procedure. This provided a set of observations for each type of tracer for each patient condition clinical group (see Table 1). Finally, the resulting set of patients is matched with the demographic information providing 531 patients.

2.2 Network Construction and Processing

2.2.1 PET Image preprocessing

Image preprocessing is carried out in two steps(see figure 1.):

1. Combining individual frames of the PET image to form a 4D raw activity image. This is done using the fslmerge utility included in FSL[23].
2. The 4D raw activity image is converted to a 4D SUV image using the following formula:
$$SUV = \frac{c_{img}}{c_{inj}} \tag{1}$$
where c_{img} (Mbq ml^{-1}) is given by the raw activity image and $c_{inj} = \frac{ID}{BW}$. ID (MBq) is the injection dose[21], and BW (g) is the body weight of the patient, considering the equivalency $1g = 1ml$
3. Spatially realigning the PET frames to correct for motion. This was done using MCFLIRT.[22] The motion correction occurs with 6 DOF. The PET frames are realigned using the mean image as a template. The mean image is obtained by applying the motion correction parameters to the time series and averaging the volumes.
4. Coregistering the 4D SUV image from subject space to MNI[58] space. This is done using FreeSurfer[44]. The image used for coregistration is the MNI152_T1_2mm_brain.

To parallelize this operation, GNU Parallel[54] is used.

2.3 PET Image-based Network Construction

The network is constructed using the regions of interest (ROIs) from the Julich Atlas[28, 14, 9]. This atlas provides 121 ROIs, which translates to 121 nodes or vertices in the network(see figure 3.). Building networks from the preprocessed images requires the generation of adjacency matrices. The adjacency matrix is computed by calculating the method described below. The Bivariate Pearson correlation performs poorly in cases of ”confounding” or ”chain” interactions. In such cases, partial correlation measures the direct connectivity between two nodes by estimating their correlation after regressing out effects from all the other nodes in the network, hence avoiding spurious effects in network modeling. Whereas in cases of ”colliding” interactions, a partial correlation may induce a spurious correlation. Thus, Sanchez-Romero and Cole have introduced a combined multiple functional connectivity method[47].

The network is constructed by computing the pairwise partial correlation values of voxel intensities in the PET images to produce an initial adjacency matrix ($matrix_{part}$). A second matrix ($matrix_{bivar}$) is constructed by computing the bivariate correlation values of voxel intensities in the PET images. Now, $matrix_{part}$ is modified using $matrix_{bivar}$ as follows:

$$matrix_{part}(i,j) = \begin{cases} 0 & if\, matrix_{bivar}(i,j) = 0 \\ no\, change & otherwise \end{cases} \tag{2}$$

where $matrix_{part}(i,j)$ and $matrix_{bivar}(i,j)$ is the element at (i,j) in the respective matrices. $matrix_{part}$ is now the combinedFC adjacency matrix that defines the network.

The partial correlation is calculated using the correlation between two residuals; the values are computed using $N-2$ ROIs as co-factors for every pair of ROIs[32]. The partial correlation values serve as the edge weights and constitute the values in the adjacency matrices.

Partial correlations are computed as correlation of residuals. The first order partial correlation ($\rho_{ij.k}$) of x_i and x_j, controlling for x_k is given by [26].

$$corr(resid(i|k), resid(j|k)) = \frac{c_{ij} - c_{ik}v_k c_{kj}}{\sqrt{v_i - c_{ik}v_k c_{ki}}\sqrt{v_j - c_{jk}v_k c_{kj}}} \tag{3}$$

where $c_{ij} = cov(x_i, x_j)$ and $v_k = var(x_k)$ Further,

$$\rho_{ij.k} = \frac{\rho_{ij} - \rho_{ik}\rho_{jk}}{\sqrt{1-\rho_{ik}^2}\sqrt{1-\rho_{jk}^2}} \tag{4}$$

Since we are controlling for $(N-2)$ ROIs for each pair of ROIs ROI_i and ROI_j, we calculate the $(N-2)^{th}$ order partial correlation. This is calculated recursively as

For each $ROI_k \in$ **ROIs**

$$\rho_{ij.\mathbf{ROIs}} = \frac{\rho_{ij.\mathbf{ROIs}\setminus\{k\}} - \rho_{ik.\mathbf{ROIs}\setminus\{k\}}\rho_{kj.\mathbf{ROIs}\setminus\{k\}}}{\sqrt{1-\rho^2_{ik.\mathbf{ROIs}\setminus\{k\}}}\sqrt{1-\rho^2_{kj.\mathbf{ROIs}\setminus\{k\}}}} \tag{5}$$

The base case of this recursive algorithm is given by equation 3. The estimation of partial correlations is a computationally intensive task, mainly due to the pre-calculation of residuals before computing cross-correlation. And because the number of covariates is large; this calculation is done in a time-optimized manner using the R package ppcor[26].

Next, the adjacency matrices are thresholded using a) data-driven thresholding scheme based on Orthogonal Minimal Spanning Trees (OMSTs)[12, 10, 27]. Network thresholding serves to remove inconsequential (or low-impact) edges and reduce the network complexity. And b) shortest path thresholding scheme [11] This is done to compare between the two common schemes used for thresholding.

The Networkx[18] Python library is used for network construction from the thresholded adjacency matrices and subsequent percolation centrality computation and other graph metrics.

2.4 Percolation Centrality Computation

Percolation centrality is a nodal metric and is calculated for each node. The percolation centrality for each node v at time t is calculated as shown below:

$$PC^t(v) = \frac{1}{(N-2)} \sum_{s \neq v \neq r} \frac{\sigma_{s,r}(v)}{\sigma_{s,r}} \frac{x_s^t}{[\sum x_v^t] - x_v^t} \tag{6}$$

Where $\sigma_{s,r}$ is the number of shortest paths between nodes s and r pass-through node v,
x_i^t is the percolation state of node i at time t,
$x_i^t = 0$ indicates a non-percolated node and,
$x_i^t = 1$ indicates a fully percolated node.

The percolation centrality value is calculated for each network using the inbuilt function of Networkx.(see supplementary data)

2.5 Collective Influence Algorithm

We define $G(q)$ the fraction of occupied sites (or nodes) belonging to the giant(largest) connected component. Percolation theory[3] tells us that if we choose these q fraction of nodes randomly, the network undergoes a structural collapse at a certain critical fraction where the probability of existence of the giant connected component vanishes, $G = 0$. The optimal percolation problem is finding the minimum fraction q_c of nodes to be removed such that $G(q_c) = 0$ i.e. the minimum fraction of "influencers" to fragment the network. For any fixed fraction $q < q_c$, we search for the configuration of removed nodes that provides the minimal non-zero giant connected component G. For further reading on how the problems of optimal immunization and spreading (optimal influencer problem) to the problem of minimizing the giant component of a network, i.e., optimal percolation problem, readers are encouraged to read [36].

The algorithm is on the basis that, given a network: the flow of information within the network is optimal with a minimum number of nodes that weigh heavily on the flow of information through the said network[37]. In the context of this investigation, the small sets of nodes/ROIs would prove to be vital in the movement of beta-amyloid plaques.

The core idea is that the overall functioning of a network in terms of the spread of information (or in our case, movement of beta-amyloid plaques) hinges on a specific set of nodes called influencers. This idea of finding the most influential nodes has been previously used in other contexts, for example, activating influential nodes in social networks to spread information[45] or de-activating or immunizing influential nodes to prevent large scale pandemics[39, 41]. In recent applications to neuroscience, this method has been used to find nodes essential for global integration of a memory network in rodents[8]. Our work is the first to apply it to study the progression of AD, to the best of our knowledge. In the context of this investigation, these small sets of influential nodes/ROIs would prove to be vital in the movement of beta-amyloid plaques.

With the implementation of Collective Influence (CI) algorithm, it facilitates to pinpoint the most influential nodes, more efficiently than previously known heuristic techniques. CI is an optimization algorithm that aims to find the minimal set of nodes that could fragment the network in optimal percolation, or in a sense, their removal would dismantle the network in many disconnected and non-extensive components. In percolation theory, if we remove nodes randomly, the network would undergo a structural collapse at a critical fraction where the probability that the giant connected

component exists is $G = 0$. The optimal percolation is an optimization problem that attempts to find the minimal fraction of influencers q to achieve the result $G(q) = 0$.

2.6 Other Graph metrics

Besides the percolation centrality measure, four other nodal metrics of a graph are calculated here. Below are the four metrics that are computed for the PET image based graphs.

2.6.1 Betweenness Centrality

The basic definition of betweenness centrality is defined as,

$$C_B(u) = \frac{\sum_{s \neq u \neq t} \frac{\partial_{st}(u)}{\partial_{st}}}{(n-1)(n-2)/2} \tag{7}$$

This centrality information provides the uniqueness of it within the network. In this study it provides the regions of interest that play a vital role in the information flow in the network; the information being beta-amyloids or tau proteins accumulation in those regions.

2.6.2 Closeness Centrality

The closeness centrality of a node denotes how close a node is in the given network. It is inversely proportional to the farness of the node. Freeman defined the closeness centrality as,

$$C_c(u) = \frac{n-1}{\sum_{\forall u, v \neq u} d(u,v)} \tag{8}$$

The distance between two nodes/ROIs u and v in a network, denoted d(u,v), is defined as the number of hops made along the shortest path between u and v. In this case, lesser the hops; closer are the two ROI's and the ease with which the misformed proteins can travel.

2.6.3 Current Flow Betweenness Centrality

Given a source ROI(s) and a target ROI(t), the absolute current flow through edge (i, j) is the quantity $A_{i,j}|v_i^{(s,t)} - v_j^{(s,t)}|$. By Kirchhoff's law the current that enters a node is equal to the current that leaves the node. Hence, the current flow $F_i^{(s,t)}$ through a node i different from the source s and a target t is half of the absolute flow on the edges incident in i:

$$F_i^{(s,t)} = \frac{1}{2} \sum_j A_{i,j} |v_i^{(s,t)} - v_j^{(s,t)}|$$

$$F_i^{(s,t)} = \frac{1}{2} \sum_j A_{i,j} |v_i^{(s,t)} - v_j^{(s,t)}|$$

Moreover, the current flows $F_s^{(s,t)}$ and $F_t^{(s,t)}$ through both s and t are set to 1, if end-points of a path are considered part of the path, or to 0 otherwise. Since the potential $v_i^{(s,t)} = G_{i,s}^+ - G_{i,t}^+$, with G^+ the generalized inverse of the graph Laplacian, the above equation can be expressed in terms of elements of G^+ as follows:

$$F_i^{(s,t)} = \frac{1}{2}\sum_j A_{i,j}|G_{i,s}^+ - G_{i,t}^+ + G_{j,t}^+ - G_{j,s}^+|$$

Finally, the current-flow betweenness centrality b_i of node i is the flow through i averaged over all source-target pairs (s,t):

$$b_i = \frac{\sum_{s<t} F_i^{(s,t)}}{(1/2)n(n-1)}$$

2.6.4 Eigenvector Centrality

Eigenvector centrality is a measure of the influence a node has on a network. If a node is pointed to by many nodes (which also have high Eigenvector centrality) then that node will have high Eigenvector centrality. In this case, the ROI's are the nodes and PET images provide the intensity value for each ROI, which helps in computing the centrality values each scan. Another interpretation to the centrality measure is that it provides the list of prominent regions in the brain network hierarchy and helps in detection of localized differences between patient populations[59].

Previous work on AD patients and comparison with normal patients provides the usefulness of Eigenvector centrality[60].

3 Statistical Analysis

For this study the null hypothesis is that percolation centrality value does not indicate the propagation of beta-amyloids within the brain network.

To determine the impact the percolation value has over each PET scan, a comparison with the regions of interest from the brain atlas is done using the Multiple linear regression analysis.

This study is exploratory in nature, and that the multiplicity problem is significant. And implementation of multiple test procedures does not solve the problem of making valid statistical inference for hypotheses that were generated by the data. But it does assist in describing the possible mechanism.

3.1 Pairwise Analysis of Variance

To obtain pairwise group differences, we carry out a post prior (post hoc) analysis using scikits-posthocs package; the Student T-test pairwise gives us the respective p values. The ANOVA test is performed for each node in the network with the null hypothesis that the mean percolation centrality of that node is the same across the three stages. To test the null hypothesis, Analysis of variance with significance level (α) of 0.05 is used.

3.2 Error Correction

To control for multiple comparisons of 121 nodes, the Scheffe Test and control for Experiment-wise Error Rate (EER) is carried out. It is a single-step procedure that calculates the simultaneous confidence intervals for all pairwise differences between means.

3.3 Multivariate Linear Regression

A correlation between the percolation centrality values for all 121 nodes and psychometric test scores - MMSE and NPIQ - is computed to identify the regions of interest that can be used as reliable predictors. Instead of performing multiple correlations across all three diagnoses, a multivariate regression analysis using regularisation techniques, wherein the features are the nodal percolation centrality values, and the target variable is the MMSE or NPIQ score. The goal is not to build a predictive model but to use it to quantify each node's influence in distinguishing between the clinical conditions for interpretation purposes. Had the purpose been building a machine learning model, it would imply the need to develop elaborate features sets (more than just percolation centrality) and utilize complex machine learning architectures (which provide less room for interpretability)

3.4 Regularization and Cross-Validation

We use regularization in our multivariate linear regression (MLR) to make sure our regression model generalizes better to unseen data. Regularization is necessary to control for overfitting. Here, both Lasso regression (L1 penalty) as well as Ridge regression (L2 penalty) are tested, and both provide similar root mean squared errors (RMSE) and similar desired results. We choose Lasso with $\alpha = 0.1$, for reporting our results (see Figure 5). To quantify the robustness and reliability of our model, before and after regularization, we perform a leave one out cross-validation (LOOCV). We choose this cross-validation strategy because it is unbiased and better suited to our smaller sample sizes (especially in PiB tracer subset). We observe an improvement in validation RMSE with an increase in regularization (parameter α), but we also observe that excessive penalization of weights at very high values of α can result in the regression model converging to the mean of the output MMSE/NPIQ scores. To take this into account, we also plot the standard deviation in predicted MMSE/NPIQ outputs and choose $\alpha = 1$ for sufficient but not excessive regularization (Further details in supplementary figures).

4 Results

4.1 Pairwise ANOVA

The student t-test is performed on the resulting five centrality values for each tracer type and clinical conditions. There was a significant effect of the beta-amyloid accumulation on the five centrality values at $p<0.05$ level for the three clinical groups[$F(3, 454) = 3.002$ for AV45 and $F(3, 97) = 3.027$ for PiB] (see Table 2).

A one-way between clinical groups ANOVA was conducted to compare the effect of beta-amyloid accumulation/tau protein on five centrality values in the cognitive normal, mild cognitive impairment and Alzheimer's disease patients(see tables 3 and 4).

4.2 Cross-Validation and Regularization

Increasing regularization (α) improves the validation RMSE (see Supplementary), making it more robust and generalize to unseen data. But at higher values of α, we see that the standard deviation of predicted MMSE scores decreases to less than $<$ 2, irrespective of clinical condition. Which could mean that it saturates to predicting the mean MMSE value when regression weights are extremely penalized. Thereby choosing a reasonably small yet effective α value (less than 2), for which the validation RMSE and the standard deviation in output predicted MMSE.

4.3 Multivariate Linear regression

A linear regression model between the percolation centrality values for all 121 nodes and psychometric test scores - MMSE and NPIQ - is computed to identify the regions of interests that can be used as reliable predictors(see figure 4.). Instead of performing multiple correlations across all three diagnoses, a multivariate regression analysis using leave one out cross validation is carried out, wherein the features are the nodal percolation centrality values and the target variable are the psychological assessment scores.(see Table 4)

4.4 Comparison of Threshold Schemes

The two schemes are compared on the number of ROI's that can be considered on the basis of ANOVA analysis($p\leq0.05$), The Juelich atlas has five clusters; frontal, parietal, temporal, occipital lobes and the white matter regions. As well as comparing the performance of the threshold schemes between the two tracers(see table 5.).

Orthogonal Minimum Spanning Tree: provides a total of 112 ROI's across the five nodal metrics. On the Basis of the tracers, 60 ROI's are obtained for AV45 and 52 for PiB. Further, the ranking of ROI on the basis of the threshold scheme is listed for the three clinical groups for the respective tracers

Shortest Path Threshold: here a total of 66 ROI's are obtained. 31 and 35 for AV45 and PiB tracers respectively. On the basis of the collective influence algorithm the ROI's are ranked for the three clinical groups and their respective tracers.

Further, comparing the number of statistically valid(MLR) ROIs across the five centrality values with the psychometric tests; MMSE and NPI-Q is performed. This helps in comparing the function of the ROI with the assessment carried out on the test(see tables 11 to 18 -supplementary information).

4.5 Other Graph Metrics

The Closeness Centrality provides the highest number of ROI's across overall; 80 in total. Eigenvector Centrality provides 33 ROI's, where as Percolation Centrality has 24 ROI's followed by the Betweenness Centrality measure with a total of 23 ROI's and Current Flow Betweenness Centrality 19 ROI's across the the two tracers(see table 5.).

4.6 Collective Influence Ranking

The collective influence algorithm ranks the ROIs; here, the rank list is generated for the two tracers- AV45 and PiB. When a comparison of the rank is carried out between the clinical groups and tracers in the case of PiB, the ranking increases when moving from CN clinical condition to MCI, and then ranking decreases going from MCI to AD. Overall the ranking increases by 50% from cognitively normal condition to Alzheimer's disease condition. A comparison of the ROIs across clinical conditions and tracers does not provide any new information at this stage regarding a common or group of common ROIs across the data(see Table 6).

4.7 Demographics

On the basis of the selection criteria, 531 patients were available for this study. Of this, 48% of the females were of the Cognitively Normal group, 25% with Mild cognitive impairment, and 27% with Alzheimer's disease.

43% of the patients received more than 12 years of education as opposed to only 16% who received less than 12 years of education, 31% received more than 12 years of education in the MCI group as opposed to 69% with less than 12 years of education.

47% of the Left-handed patients were in the AD clinical group as opposed to 26% in the right-handed patients. One patient in the MCI, two in CN, and four in AD groups were multilingual.

5 Discussion

Here, a comparison of five nodal metrics; Betweenness centrality, closeness centrality, current flow betweenness centrality, Eigenvector centrality, and percolation cen-

trality is carried out to better understand the study. Based on the variance analysis and multivariate regression testing and the percolation centrality graph metric computed using the PET images, it is possible to show Alzheimer's disease progressing through the beta-amyloid/tau protein networks.

The student t-test provides nodes for each of the five centrality measures across the three clinical conditions, tracer types, and threshold schemes. Here, only the Current Flow Betweenness Centrality Measure fails to provide ROIs across all conditions (see tables 6 through 10), provides only 3 in cognitively normal condition and two in a mild cognitively impaired condition, both using the OMST scheme for threshold.

It is observed that percolation centrality values of certain areas of the brain, such as inferior and superior parietal lobules, are reliable for the tracer PiB. In contrast, for most other cases, the brain areas differ for each tracer considerably. The variation due to the tracers could be because AV45 and PiB bind to the amyloids. It is also observed that the percolation centrality of Broca's area is a reliable differentiator between CN and AD clinical conditions, which validates previous findings that cognitive impairment affects speech production[16].

The MLR analysis for each of the centrality measures across the clinical conditions for both the tracer types provides, on average, one to two ROIs across conditions that can be considered as markers for studying Alzheimer's disease. Expect the current flow betweenness centrality measure, which performed poorly in this study providing only four(3-CN, 1-MCI) ROIs for both the threshold schemes and only one(MCI) ROI for AV45 and PiB tracers, respectively.

Further, when MLR is carried out for the NPI questionnaire, it provides fewer ROIs for each of the centrality measures. When comparing the contribution of ROIs for MMSE-related tasks and NPIQ related tasks. Percolation centrality has the highest percentage of 41% of ROIs. Followed by Closeness centrality with 40.5%, Betweenness centrality with 30%.

The collective influence algorithm yields nine rank lists. These tables contain the ranking of the nodes, from most influential to least, for each patient condition and type of tracer used(see Figure 5). Moreover, since the influential nodes are identified using optimal percolation theory, it validates percolation centrality as a potential metric for diagnosis. Furthermore, ROIs that could be a potential indicator of Alzheimer's disease progression across the clinical conditions and tracers can be identified by creasing the number of samples. On the comparison of the rank list for the two threshold schemes, it is observed that the occurrences of the ROI's are higher in the OMST scheme than in the SPT scheme.

The results from the Scheffe test provide a means to validate and increase the confidence in the results—the leave one out cross-validation (LOOCV) strategy to test the robustness and reliability of our regression. Here cross-validation strategy is implemented because it is unbiased and better suited to our smaller sample size. Using the regularization (L1 - Lasso or L2 - Ridge) to control for overfitting, it is observed that increasing regularization on validation RMSE.

The ROIs obtained from the pairwise t-test for between the clinical conditions show that OMST scheme provides a higher number of valid ROIs across the five centrality measures. On comparison between the two tracer types and threshold schemes;

AV45 provides 92 ROIs, whereas PiB gives 88 ROIs. Of this, 33.7% and 39.8% of the ROIs are based on the Shortest Path threshold scheme.

Previous studies show that the seeding of amyloid-beta occurs in neocortical and subcortical regions[25], from this study it is observed that for PiB the following ROI - WM Superior occipito-frontal fascicle R is part of both the neocortical and subcortical regions of the brain. Apart from this, AV45 tracer has GM Medial geniculate body L ROI in the subcortical region and the following in the neocortical region -GM Superior parietal lobule 7P L, GM Anterior intra-parietal sulcus hIP3 R, GM Superior parietal lobule 7A L and GM Superior parietal lobule 5L L, these are picked up with OMST scheme across all conditions when compared to SPT.

Prior research shows that damage to the parietal lobe is common in AD, which can lead to apraxia[16, 29], which is attested by these results. AD is associated with atrophy of the cornu ammonis, the subfield of the hippocampus, and deficits in episodic memory and spatial orientation[2, 33, 40].

And the following in the the subcortical region - GM Amygdala-laterobasal group L, GM Amygdala-laterobasal group R and GM Hippocampus hippocampal-amygdaloid transition area R. Age factor not so important but the presence of beta amyloid deposits is[19], Since these ROIs stand out irrespective of the clinical condition or demographic backgrounds, the percolation centrality has a potential to be a reliable value for AD diagnosis, these ROIs are picked up by both tracers and threshold schemes.

This study's demographic does not provide enough knowledge into the possible advantages or disadvantages that environmental or lifestyle provide for beta-amyloid percolation. This is largely due to the small sample size, and the distribution of data points within the clinical groups is asymmetric.

The intensity of a voxel/node is used to determine if the node is percolated or not; a higher intensity signifies a percolated node, and zero or lower intensity signifies an ability to permeate with ease (See Figure 2).

5.1 Limitations

This study does not give any evidence regarding the disease progression in terms of the ROIs or patient clinical group. However, this can be addressed by increasing the number of observations within each patient clinical group.

The PET tracers used for acquiring the images, Pittsburgh Compound B (PiB) and Florbetapir (AV45), are compared to check for which among the two tracers provide a more consistent or reliable PCv. Here, the AV45 tracer binds with a high affinity to the beta-amyloid plaque, whereas PiB binds to oligomers or protofibrils. A possible explanation for the difference in PCv generated using these tracers would be their binding targets. The use of second-generation tracers can help improve the accuracy and test the applicability of percolation centrality on other neurodegenerative diseases and the possibility of using it in metastatic cancer scenarios.

Expanding the dataset to include more patients and comprehensive data that factors in healthy aging shrinkage of the brain, which results in a decrease of the distances of the brain networks, can help improve the reliability of the percolation cen-

trality value. This can then provide a setting for testing out other psychological assessments that can be used as early indicators for dementia due to Alzheimer's disease, thereby tailoring it to specific demographics or population subsets.

The current pipeline is built for tracers such as AV45 and PiB, which indicate beta-amyloid plaque concentrations directly and as a posthoc implementation. However, the pipeline can work with a second generation tracers and tracers like FDG with some appropriate modifications, namely: taking the multiplicative inverse of the percolation states of each of the ROIs to reflect the behavior of the FDG tracer.

6 Conclusion

This study shows that percolation centrality is a reliable predictor and identifies the nodes that regulate the movement of beta-amyloid plaque and use them to track the disease.

This work demonstrates that using the existing neuroimaging method, PET-CT, can add value with relatively short computation time provided sufficient hardware capability is present. The ability to provide a metric to the extent of the disease state is advantageous to the current world of Alzheimer's. Prolonging life with modern-day medicine pushes patients to a world of medical experiences that deviate from the normal. Being able to show the deviation with a value such as percolation centrality has potential applications.

The reliability of percolation centrality can be improved by addressing the concerns that arise by the factors such as the number of patients and the number of patients within each clinical group, time points of data collection, demographics, and the PET tracers used were the limiting factors. Thus, this study provides the usability of percolation centrality value to determine the patient's state and sets the stage for studying other neurodegenerative diseases.

Unlike measures such as hub centrality or betweenness centrality, which provide information regarding a vital vertex/node within a network, the collective influence algorithm provides a minimum set of nodes of the network that are key to the beta-amyloid plaque movement, which can provide information regarding a particular pathway that is susceptible to the disease.

The threshold schemes implemented in this study indicate that a data-driven approach such as the Orthogonal Minimum Spanning Tree provides better results compared to the Shortest Path approach. Finally, we rank the ROIs based on influence in the network using the CI algorithm. We compare the results on two thresholding approaches, SPT and OMST, along with finding the influential nodes; this will help us gauge the reliability across different threshold schemes. CI algorithm gives a ranked list of influential nodes for each network (or each scan). The rank of a node is then further calculated for each category as the sum of individuals ranks of that node for every scan-wise list, divided by the number of scans it occurs in. Nodes are then ranked accordingly in a given category. This provides a general ranking of nodes in a category (AD/MCI/CN) instead of looking at influential nodes in each scan separately. The results differ slightly based on the thresholding scheme adopted but broadly align with MLR results discussed earlier. Since this is an exploratory study,

improving robustness across different thresholding schemes can be a possible future work.

7 Figures and Tables

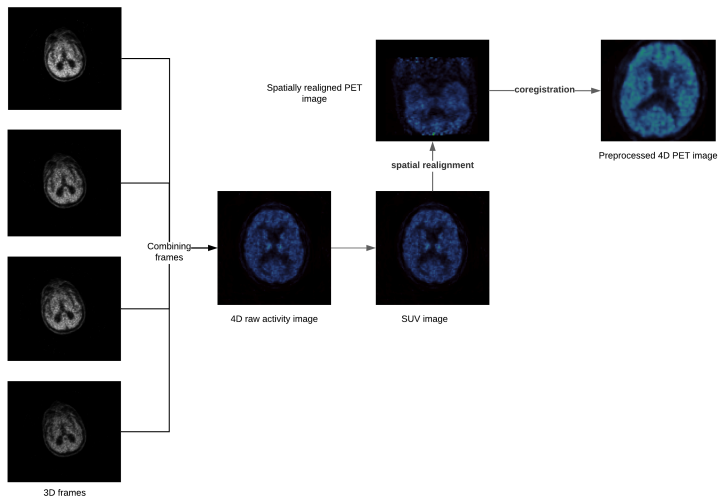

Fig. 1 PET image preprocessing flowchart.

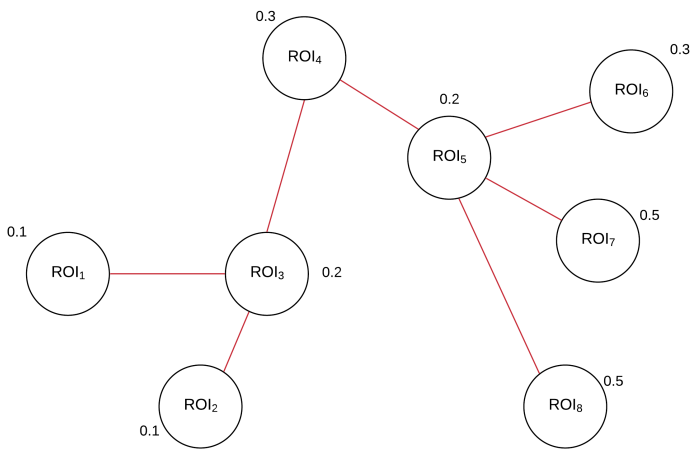

Fig. 2 Generic example of a Percolation Network and Percolation Centrality

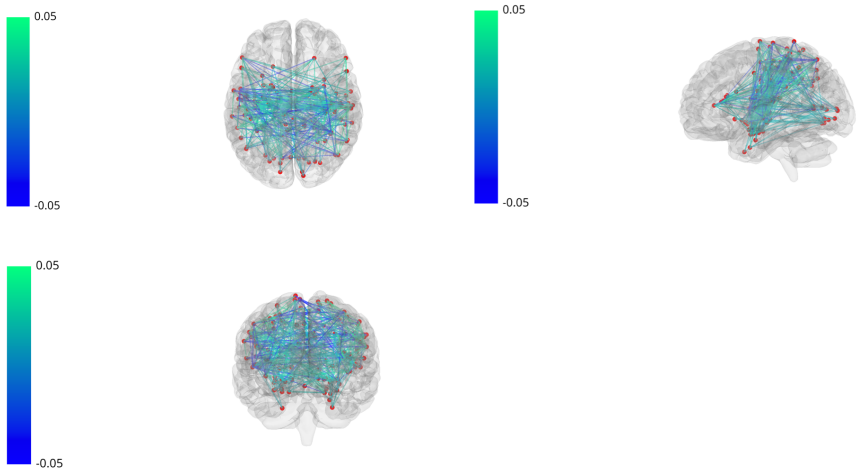

Fig. 3 A connected network of all the nodes using the Julich Atlas. Green circles indicate the ROIs, the connecting lines indicate the edges with their weights as denoted by the accompanying color bar

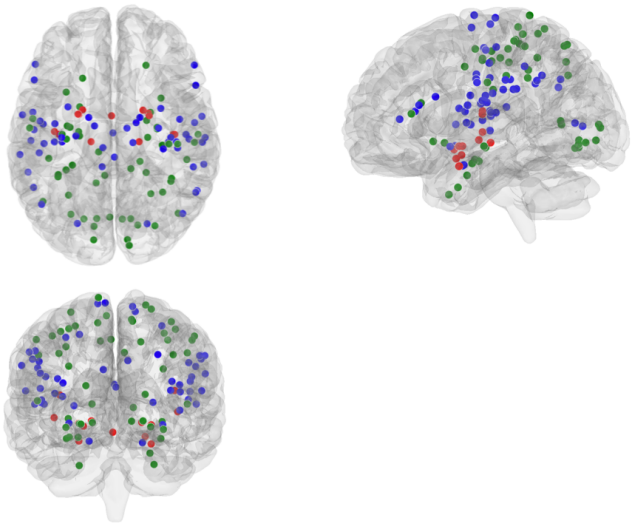

Fig. 4 Illustrates the ROIs that corresponds to MMSE and NPIQ. The green circles represent ROIs associated with the MMSE psychometric assessment, the red circles represent ROIs associated with the NPIQ psychometric assessment, and the blue circles represent ROIs associated with both MMSE and NPIQ

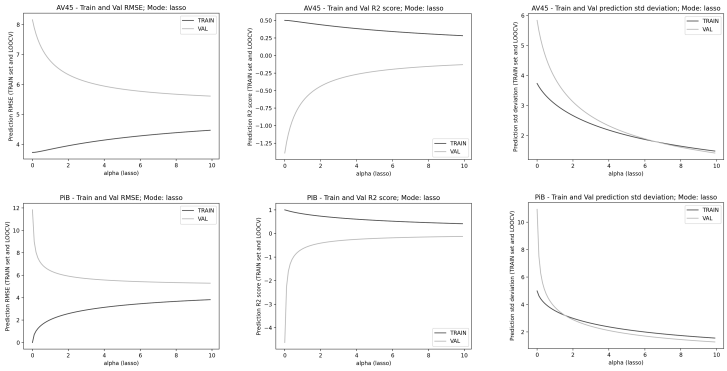

Fig. 5 Regularization using Lasso regression with L1 penalty.

Table 1 Distribution of patients

CN		**MCI**		**AD**	
AV45	PiB	AV45	PiB	AV45	PiB
262	13	76	65	116	19
M - 122 F - 140	M - 8 F - 5	M - 54 F - 22	M - 45 F - 20	M - 67 F - 49	M - 11 F - 8
Total - 275; M - 130, F - 145		Total - 141; M - 99, F - 42		Total - 135; M - 78, F - 57	

Table 2 Number of Scans per tracer type and corresponding critical F-values

Tracer	**AV45**	**PiB**
No. of scans	454	97
Critical F-value	3.002	3.027

CN: Cognitively Normal, MCI: Mild Cognitive Impairment, AD: Alzheimer's Disease, M: Male, F: Female

Table 3 Pairwise ANOVA for AV45 & PiB tracers for Betweenness Centrality

Tracer Type		AV45		PiB		
Threshold Scheme	Region of Interest(ROI)	f Value	p value	ROI	f Value	p value
OMST	GM Premotor cortex BA6 R	5.94058	0.00283	GM Broca's area BA45 R	5.17524	0.00737
	GM Hippocampus subiculum L	4.96071	0.00737	GM Broca's area BA45 L	4.75064	0.01082
	GM Visual cortex V5 L	4.39253	0.01288	GM Anterior intra-parietal sulcus hIP3 R	3.79311	0.02604
	GM Superior parietal lobule 7M L	4.34316	0.01352	GM Broca's area BA44 L	3.41148	0.03712
	GM Primary motor cortex BA4a L	3.73310	0.02463	GM Mamillary body	3.28403	0.041819
	GM Primary somatosensory cortex BA1 R	3.56446	0.02908			
	GM Primary auditory cortex TE1.2 R	3.313344	0.03724			
Shortest Path	GM Insula Ig2 L	4.58606	0.01065	GM Broca's area BA44 R	6.22322	0.00289
	WM Acoustic radiation R	4.20148	0.01553	GM Primary auditory cortex TE1.2 R	5.14313	0.00759
	GM Hippocampus subiculum L	3.89670	0.02096	WM Cingulum R	4.61276	0.01227
	GM Mamillary body	3.63729	0.02706	GM Inferior parietal lobule PFcm R	3.96185	0.02228
	GM Inferior parietal lobule Pga R	3.04114	0.04872			

Table 4 Pairwise ANOVA for AV45 & PiB tracers for Percolation Centrality

Tracer Type	AV45			PiB		
Threshold Scheme	ROI	f value	p Value	ROI	f value	p Value
OMST	GM Premotor cortex BA6 R	5.87527	0.00301	GM Broca's area BA45 R	5.14526	0.00757
	GM Hippocampus subiculum L	4.85878	0.00815	GM Broca's area BA45 L	4.82933	0.01008
	GM Superior parietal lobule 7M L	4.48842	0.01172	GM Anterior intra-parietal sulcus hIP3 R	3.87540	0.02413
	GM Visual cortex V5 L	4.38406	0.01298	GM Broca's area BA44 L	3.42666	0.03660
	GM Anterior intra-parietal sulcus hIP1 L	4.14044	0.01650	GM Mamillary body	3.33030	0.04005
	GM Superior parietal lobule 7P R	3.83169	0.02235			
	GM Primary motor cortex BA4a L	3.77498	0.02363			
	GM Primary somatosensory cortex BA1 R	3.65131	0.02669			
	GM Primary auditory cortex TE1.2 R	3.34477	0.03610			
SPT	GM Insula Ig2 L	4.64660	0.01003	GM Broca's area BA44 R	6.30152	0.00270
	WM Acoustic radiation R	4.38387	0.01299	GM Primary auditory cortex TE1.2 R	5.03630	0.00835
	GM Hippocampus subiculum L	3.93751	0.02014	WM Cingulum R	4.57068	0.01275
	GM Mamillary body	3.54618	0.02960	GM Inferior parietal lobule PFcm R	3.94533	0.02263
	GM Inferior parietal lobule Pga R	3.17572	0.04266			
	GM Lateral geniculate body L	3.05960	0.04784			

Table 5 Distribution of ROI's across graph metrics and tracer type on the basis of ANOVA test.

Threshold Scheme	OMST		SPT	
Tracer/ Centrality Measure	AV45	PiB	AV45	PiB
BC	9	5	5	4
CC	33	29	10	6
CFBC	5	2	1	12
EVC	4	11	9	9
PC	9	5	6	4

BC: Betweenness Centrality, CC: Closeness Centrality, CFBC: Current Flow Betweenness Centrality, EVC: Eigenvector Centrality and PC: Percolation Centrality

Table 6 Multivariate Linear Regression Analysis- Number of Region of Interest Across Clinical Conditions for Both Threshold Schemes for Betweenness Centrality

	Clinical Condition		CN		MCI		AD	
Graph Metric	PT	Tracer	OMST	SPT	OMST	SPT	OMST	SPT
Betweenness Centrality	MMSE	AV45	4	5	13	8	4	7
		PiB	5	4	5	1	2	9
	NPI-Q	AV45	0	3	1	1	0	0
		PiB	2	14	1	0	3	10

Table 7 Multivariate Linear Regression Analysis- Number of Region of Interest Across Clinical Conditions for Both Threshold Schemes for Percolation Centrality

	Clinical Condition		CN		MCI		AD	
Graph Metric	PT	Tracer	OMST	SPT	OMST	SPT	OMST	SPT
Percolation Centrality	MMSE	AV45	4	6	12	2	4	7
		PiB	5	3	5	0	2	9
	NPI-Q	AV45	6	3	2	1	0	0
		PiB	2	14	0	1	3	10

PT: Psychometric Assessment, OMST: Orthogonal Minimum Spanning Tree, SPT: Shortest Path Threshold, MMSE: Mini Mental State Examination, NPIQ: Neuropsychiatric Inventory Questionnaire Questionnaire

Conflict of interest

The authors declare that they have no conflict of interest.

References

1. (2020). 2020 Alzheimer's disease facts and figures. *Alzheimer's and Dementia*, 16(3):391–460.
2. Adler, D. H., Wisse, L. E., Ittyerah, R., Pluta, J. B., Ding, S. L., Xie, L., Wang, J., Kadivar, S., Robinson, J. L., Schuck, T., Trojanowski, J. Q., Grossman, M., Detre, J. A., Elliott, M. A., Toledo, J. B., Liu, W., Pickup, S., Miller, M. I., Das, S. R., Wolk, D. A., and Yushkevich, P. A. (2018). Characterizing the human hippocampus in aging and Alzheimer's disease using a computational atlas derived from ex vivo MRI and histology. *Proceedings of the National Academy of Sciences of the United States of America*, 115(16):4252–4257.
3. Bollobás, B., Bollobás, B., Riordan, O., and Riordan, O. (2006). *Percolation*. Cambridge University Press.
4. Chopra, A., Shan, L., Eckelman, W. C., Leung, K., Latterner, M., Bryant, S. H., and Menkens, A. (2012). Molecular Imaging and Contrast Agent Database (MICAD): evolution and progress. *Molecular imaging and biology*, 14(1):4–13.
5. Chung, J., Yoo, K., Kim, E., Na, D. L., and Jeong, Y. (2016). Glucose Metabolic Brain Networks in Early-Onset vs. Late-Onset Alzheimer's Disease .
6. Cummings, J. L., Mega, M., Gray, K., Rosenberg-Thompson, S., Carusi, D. A., and Gornbein, J. (1994). The Neuropsychiatric Inventory: comprehensive assessment of psychopathology in dementia. *Neurology*, 44(12):2308–2314.
7. de Haan, W., Mott, K., van Straaten, E. C., Scheltens, P., and Stam, C. J. (2012). Activity Dependent Degeneration Explains Hub Vulnerability in Alzheimer's Disease. *PLoS Computational Biology*, 8(8).

8. Del Ferraro, G., Moreno, A., Min, B., Morone, F., Pérez-Ramírez, Ú., Pérez-Cervera, L., Parra, L. C., Holodny, A., Canals, S., and Makse, H. A. (2018). Finding influential nodes for integration in brain networks using optimal percolation theory. *Nature Communications*, 9(1).
9. Desikan, R. S., Ségonne, F., Fischl, B., Quinn, B. T., Dickerson, B. C., Blacker, D., Buckner, R. L., Dale, A. M., Maguire, R. P., Hyman, B. T., Albert, M. S., and Killiany, R. J. (2006). An automated labeling system for subdividing the human cerebral cortex on MRI scans into gyral based regions of interest. *NeuroImage*, 31(3):968–980.
10. Dimitriadis, S. I., Antonakakis, M., Simos, P., Fletcher, J. M., and Papanicolaou, A. C. (2017a). Data-Driven Topological Filtering Based on Orthogonal Minimal Spanning Trees: Application to Multigroup Magnetoencephalography Resting-State Connectivity. *Brain connectivity*, 7(10):661–670.
11. Dimitriadis, S. I., Laskaris, N. A., Tsirka, V., Vourkas, M., Micheloyannis, S., and Fotopoulos, S. (2010). Tracking brain dynamics via time-dependent network analysis. *Journal of Neuroscience Methods*, 193(1):145–155.
12. Dimitriadis, S. I., Salis, C., Tarnanas, I., and Linden, D. E. (2017b). Topological Filtering of Dynamic Functional Brain Networks Unfolds Informative Chronnectomics: A Novel Data-Driven Thresholding Scheme Based on Orthogonal Minimal Spanning Trees (OMSTs) .
13. Dubois, B., Slachevsky, A., Litvan, I., and Pillon, B. (2000). The FAB: a Frontal Assessment Battery at bedside. *Neurology*, 55(11):1621–1626.
14. Eickhoff, S. B., Stephan, K. E., Mohlberg, H., Grefkes, C., Fink, G. R., Amunts, K., and Zilles, K. (2005). A new SPM toolbox for combining probabilistic cytoarchitectonic maps and functional imaging data. *NeuroImage*, 25(4):1325–1335.
15. El-Hayek, Y. H., Wiley, R. E., Khoury, C. P., Daya, R. P., Ballard, C., Evans, A. R., Karran, M., Molinuevo, J. L., Norton, M., and Atri, A. (2019). Tip of the Iceberg: Assessing the Global Socioeconomic Costs of Alzheimer's Disease and Related Dementias and Strategic Implications for Stakeholders. *Journal of Alzheimer's Disease*, 70:1–19.
16. Fernández, M., Gobartt, A. L., Balañá, M., and Group, C. S. (2010). Behavioural symptoms in patients with Alzheimer's disease and their association with cognitive impairment. *BMC neurology*, 10:87.
17. Gupta, Y., Lama, R. K., Kwon, G.-R., Weiner, M. W., Aisen, P., Weiner, M., Aisen, P., Petersen, R., Jack, C. R., Jagust, W., Trojanowki, J. Q., Toga, A. W., Beckett, L., Green, R. C., Saykin, A. J., Morris, J., Shaw, L. M., Khachaturian, Z., Sorensen, G., Carrillo, M., Kuller, L., Raichle, M., Paul, S., Davies, P., Fillit, H., Hefti, F., Holtzman, D., Mesulam, M. M., Potter, W., Snyder, P., Schwartz, A., Green, R. C., Montine, T., Petersen, R., Aisen, P., Thomas, R. G., Donohue, M., Walter, S., Gessert, D., Sather, T., Jiminez, G., Balasubramanian, A. B., Mason, J., Sim, I., Beckett, L., Harvey, D., Donohue, M., Jack, C. R., Bernstein, M., Fox, N., Thompson, P., Schuff, N., DeCArli, C., Borowski, B., Gunter, J., Senjem, M., Vemuri, P., Jones, D., Kantarci, K., Ward, C., Jagust, W., Koeppe, R. A., Foster, N., Reiman, E. M., Chen, K., Mathis, C., Landau, S., Morris, J. C., Cairns, N. J., Franklin, E., Taylor-Reinwald, L., Shaw, L. M., Trojanowki, J. Q., Lee, V., Korecka, M., Figurski, M., Toga, A. W., Crawford, K., Neu, S., Saykin, A. J., Foroud, T. M., Potkin, S., Shen, L., Faber, K., Kim, S., Nho, K., Weiner, M. W., Thal, L., Khachaturian, Z., Thal, L., Buckholtz, N., Weiner, M. W., Snyder, P. J., Potter, W., Paul, S., Albert, M., Frank, R., Khachaturian, Z., Hsiao, J., Kaye, J., Quinn, J., Silbert, L., Lind, B., Carter, R., Dolen, S., Schneider, L. S., Pawluczyk, S., Becerra, M., Teodoro, L., Spann, B. M., Brewer, J., Vanderswag, H., Fleisher, A., Heidebrink, J. L., Lord, J. L., Petersen, R., Mason, S. S., Albers, C. S., Knopman, D., Johnson, K., Doody, R. S., Villanueva-Meyer, J., Pavlik, V., Shibley, V., Chowdhury, M., Rountree, S., Dang, M., Stern, Y., Honig, L. S., Bell, K. L., Ances, B., Morris, J. C., Carroll, M., Creech, M. L., Franklin, E., Mintun, M. A., Schneider, S., Oliver, A., Marson, D., Geldmacher, D., Natelson Love, M., Griffith, R., Clark, D., Brockington, J., Roberson, E., Grossman, H., Mitsis, E., Shah, R. C., DeToledo-Morrell, L., Duara, R., Greig-Custo, M. T., Barker, W., Albert, M., Onyike, C., D'Agostino, D., Kielb, S., Sadowski, M., Sheikh, M. O., Anaztasia, U., Mrunalini, G., Doraiswamy, P. M., Petrella, J. R., Borges-Neto, S., Wong, T. Z., Coleman, E., Arnold, S. E., Karlawish, J. H., Wolk, D. A., Clark, C. M., Smith, C. D., Jicha, G., Hardy, P., Sinha, P., Oates, E., Conrad, G., Lopez, O. L., Oakley, M., Simpson, D. M., Porsteinsson, A. P., Goldstein, B. S., Martin, K., Makino, K. M., Ismail, M. S., Brand, C., Potkin, S. G., Preda, A., Nguyen, D., Womack, K., Mathews, D., Quiceno, M., Levey, A. I., Lah, J. J., Cellar, J. S., Burns, J. M., Swerdlow, R. H., Brooks, W. M., Apostolova, L., Tingus, K., Woo, E., Silverman, D. H. S., Lu, P. H., Bartzokis, G., Graff-Radford, N. R., Parfitt, F., Poki-Walker, K., Farlow, M. R., Hake, A. M., Matthews, B. R., Brosch, J. R., Herring, S., van Dyck, C. H., Carson, R. E., MacAvoy, M. G., Varma, P., Chertkow, H., Bergman, H., Hosein, C., Black, S., Stefanovic, B., Caldwell, C., Hsiung, G.-Y. R., Mudge, B., Sossi, V., Feldman, H., Assaly, M., Finger, E., Pasternack, S., Rachisky, I., Trost, D., Kertesz, A., Bernick, C., Munic, D., Mesulam, M.-M., Rogalski, E., Lipowski,

K., Weintraub, S., Bonakdarpour, B., Kerwin, D., Wu, C.-K., Johnson, N., Sadowsky, C., Villena, T., Turner, R. S., Johnson, K., Reynolds, B., Sperling, R. A., Johnson, K. A., Marshall, G., Yesavage, J., Taylor, J. L., Lane, B., Rosen, A., Tinklenberg, J., Sabbagh, M. N., Belden, C. M., Jacobson, S. A., Sirrel, S. A., Kowall, N., Killiany, R., Budson, A. E., Norbash, A., Johnson, P. L., Obisesan, T. O., Wolday, S., Allard, J., Lerner, A., Ogrocki, P., Tatsuoka, C., Fatica, P., Fletcher, E., Maillard, P., Olichney, J., DeCarli, C., Carmichael, O., Kittur, S., Borrie, M., Lee, T.-Y., Bartha, R., Johnson, S., Asthana, S., Carlsson, C. M., Potkin, S. G., Preda, A., Nguyen, D., Tariot, P., Burke, A., Milliken, A. M., Trncic, N., Fleisher, A., Reeder, S., Bates, V., Capote, H., Rainka, M., Scharre, D. W., Kataki, M., Kelley, B., Zimmerman, E. A., Celmins, D., Brown, A. D., Pearlson, G. D., Blank, K., Anderson, K., Flashman, L. A., Seltzer, M., Hynes, M. L., Santulli, R. B., Sink, K. M., Leslie, G., Williamson, J. D., Garg, P., Watkins, F., Ott, B. R., Tremont, G., Daiello, L. A., Salloway, S., Malloy, P., Correia, S., Rosen, H. J., Miller, B. L., Perry, D., Mintzer, J., Spicer, K., Bachman, D., Finger, E., Pasternak, S., Rachinsky, I., Rogers, J., Kertesz, A., Drost, D., Pomara, N., Hernando, R., Sarrael, A., Schultz, S. K., Smith, K. E., Koleva, H., Nam, K. W., Shim, H., Relkin, N., Chiang, G., Lin, M., Ravdin, L., Smith, A., Raj, B. A., Fargher, K., Weiner, M. W., Aisen, P., Weiner, M., Aisen, P., Petersen, R., Green, R. C., Harvey, D., Jack, C. R., Jagust, W., Morris, J. C., Saykin, A. J., Shaw, L. M., Toga, A. W., Trojanowki, J. Q., Neylan, T., Grafman, J., Green, R. C., Montine, T., Weiner, M., Petersen, R., Aisen, P., Thomas, R. G., Donohue, M., Devon, G., Sather, T., Melissa, D., Morrison, R., Jiminez, G., Neylan, T., Jacqueline, H., Shannon, F., Harvey, D., Donohue, M., Jack, C. R., Bernstein, M., Borowski, B., Gunter, J., Senjem, M., Kejal, K., Chad, W., Jagust, W., Koeppe, R. A., Foster, N., Reiman, E. M., Chen, K., Landau, S., Morris, J. C., Cairns, N. J., Householder, E., Shaw, L. M., Trojanowki, J. Q., Lee, V., Korecka, M., Figurski, M., Toga, A. W., Karen, C., Scott, N., Saykin, A. J., Foroud, T. M., Potkin, S., Shen, L., Faber, K., Kim, S., Nho, K., Weiner, M. W., Karl, F., Schneider, L. S., Pawluczyk, S., Mauricio, B., Brewer, J., Vanderswag, H., Stern, Y., Honig, L. S., Bell, K. L., Fleischman, D., Arfanakis, K., Shah, R. C., Duara, R., Varon, D., Greig, M. T., Doraiswamy, P. M., Petrella, J. R., James, O., Porsteinsson, A. P., Goldstein, B., Martin, K. S., Potkin, S. G., Preda, A., Nguyen, D., Mintzer, J., Massoglia, D., Brawman-Mintzer, O., Sadowsky, C., Martinez, W., Villena, T., Jagust, W., Landau, S., Rosen, H., Perry, D., Turner, R. S., Behan, K., Reynolds, B., Sperling, R. A., Johnson, K. A., Marshall, G., Sabbagh, M. N., Jacobson, S. A., Sirrel, S. A., Obisesan, T. O., Wolday, S., Allard, J., Johnson, S. C., Fruehling, J. J., Harding, S., Peskind, E. R., Petrie, E. C., Li, G., Yesavage, J. A., Taylor, J. L., Furst, A. J., Chao, S., Relkin, N., Chiang, G., Ravdin, L., Ravdin, L., Mackin, S., Aisen, P., Raman, R., Mackin, S., Weiner, M., Aisen, P., Raman, R., Jack, C. R., Landau, S., Saykin, A. J., Toga, A. W., DeCarli, C., Koeppe, R. A., Green, R. C., Drake, E., Weiner, M., Aisen, P., Raman, R., Donohue, M., Jimenez, G., Gessert, D., Harless, K., Salazar, J., Cabrera, Y., Walter, S., Hergesheimer, L., Shaffer, E., Mackin, S., Nelson, C., Bickford, D., Butters, M., Zmuda, M., Jack, C. R., Bernstein, M., Borowski, B., Gunter, J., Senjem, M., Kantarci, K., Ward, C., Reyes, D., Koeppe, R. A., Landau, S., Toga, A. W., Crawford, K., Neu, S., Saykin, A. J., Foroud, T. M., Faber, K. M., Nho, K., Nudelman, K. N., Mackin, S., Rosen, H., Nelson, C., Bickford, D., Au, Y. H., Scherer, K., Catalinotto, D., Stark, S., Ong, E., Fernandez, D., Butters, M., Zmuda, M., Lopez, O. L., Oakley, M., and Simpson, D. M. (2019). Prediction and Classification of Alzheimer's Disease Based on Combined Features From Apolipoprotein-E Genotype, Cerebrospinal Fluid, MR, and FDG-PET Imaging Biomarkers .

18. Hagberg, A. A., Schult, D. A., and Swart, P. J. (2008). Exploring Network Structure, Dynamics, and Function using NetworkX. In Varoquaux, G., Vaught, T., and Millman, J., editors, *Proceedings of the 7th Python in Science Conference*, pages 11–15, Pasadena, CA USA.
19. Hamaguchi, T., Eisele, Y. S., Varvel, N. H., Lamb, B. T., Walker, L. C., and Jucker, M. (2012). The presence of aβ seeds, and not age per se, is critical to the initiation of aβ deposition in the brain. *Acta Neuropathologica*, 123(1):31–37.
20. Holtzman, D. M., Herz, J., and Bu, G. (2012). Apolipoprotein E and apolipoprotein E receptors: normal biology and roles in Alzheimer disease. *Cold Spring Harbor perspectives in medicine*, 2(3):a006312.
21. Initiative, A. D. N. (2017). Pet acquisition.
22. Jenkinson, M., Bannister, P., Brady, M., and Smith, S. (2002). Improved optimization for the robust and accurate linear registration and motion correction of brain images. *NeuroImage*, 17(2):825 – 841.
23. Jenkinson, M., Beckmann, C. F., Behrens, T. E. J., Woolrich, M. W., and Smith, S. M. (2012). FSL. *NeuroImage*, 62(2):782–790.
24. Johnson, K. A., Minoshima, S., Bohnen, N. I., Donohoe, K. J., Foster, N. L., Herscovitch, P., Karlawish, J. H., Rowe, C. C., Carrillo, M. C., Hartley, D. M., Hedrick, S., Pappas, V., and Thies, W. H. (2013). Appropriate use criteria for amyloid PET: a report of the Amyloid Imaging Task Force, the Society of

Nuclear Medicine and Molecular Imaging, and the Alzheimer's Association. *Alzheimer's & dementia : the journal of the Alzheimer's Association*, 9(1):e–1–16.
25. Jucker, M. and Walker, L. C. (2013). Self-propagation of pathogenic protein aggregates in neurodegenerative diseases. *Nature*, 501(7465):45–51.
26. Kim, S. (2015). ppcor: An R Package for a Fast Calculation to Semi-partial Correlation Coefficients. *Communications for Statistical Applications and Methods*, 22(6):665–674.
27. Klyuzhin, I. S., Fu, J. F., Hong, A., Sacheli, M., Shenkov, N., Matarazzo, M., Rahmim, A., Jon Stoessl, A., and Sossi, V. (2018). Data-driven, voxel-based analysis of brain PET images: Application of PCA and LASSO methods to visualize and quantify patterns of neurodegeneration. *PLoS ONE*, 13(11):1–20.
28. Kötter, R., Mazziotta, J., Toga, A., Evans, A., Fox, P., Lancaster, J., Zilles, K., Woods, R., Paus, T., Simpson, G., Pike, B., Holmes, C., Collins, L., Thompson, P., MacDonald, D., Iacoboni, M., Schormann, T., Amunts, K., Palomero-Gallagher, N., Geyer, S., Parsons, L., Narr, K., Kabani, N., Goualher, G. L., Boomsma, D., Cannon, T., Kawashima, R., and Mazoyer, B. (2001). A probabilistic atlas and reference system for the human brain: International Consortium for Brain Mapping (ICBM). *Philosophical Transactions of the Royal Society of London. Series B: Biological Sciences*, 356(1412):1293–1322.
29. Kueper, J. K., Speechley, M., Lingum, N. R., and Montero-Odasso, M. (2017). Motor function and incident dementia: a systematic review and meta-analysis. *Age and Ageing*, 46(5):729–738.
30. Landau, S. M., Thomas, B. A., Thurfjell, L., Schmidt, M., Margolin, R., Mintun, M., Pontecorvo, M., Baker, S. L., Jagust, W. J., and Initiative, A. D. N. (2014). Amyloid PET imaging in Alzheimer's disease: a comparison of three radiotracers. *European journal of nuclear medicine and molecular imaging*, 41(7):1398–1407.
31. Loy, C. T., Schofield, P. R., Turner, A. M., and Kwok, J. B. J. (2014). Genetics of dementia. *Lancet (London, England)*, 383(9919):828–840.
32. Madigan, D. (1994). Graphical models in applied multivariate statistics, by J. Whittaker, John Wiley & Sons, New York, 1990, 448 pp. Price: $59.95. *Networks*, 24(2):125.
33. Masurkar, A. V. (2018). Towards a circuit-level understanding of hippocampal CA1 dysfunction in Alzheimer's disease across anatomical axes. *Journal of Alzheimer's disease & Parkinsonism*, 8(1):412.
34. McKhann, G. M., Knopman, D. S., Chertkow, H., Hyman, B. T., Jack, C. R. J., Kawas, C. H., Klunk, W. E., Koroshetz, W. J., Manly, J. J., Mayeux, R., Mohs, R. C., Morris, J. C., Rossor, M. N., Scheltens, P., Carrillo, M. C., Thies, B., Weintraub, S., and Phelps, C. H. (2011). The diagnosis of dementia due to Alzheimer's disease: recommendations from the National Institute on Aging-Alzheimer's Association workgroups on diagnostic guidelines for Alzheimer's disease. *Alzheimer's & dementia : the journal of the Alzheimer's Association*, 7(3):263–269.
35. Moore, C. and Newman, M. E. J. (2000). Epidemics and percolation in small-world networks. *Physical Review E*, 61(5):5678–5682.
36. Morone, F. and Makse, H. A. (2015). Influence maximization in complex networks through optimal percolation. *Nature*, 524(7563):65–68.
37. Morone, F., Min, B., Bo, L., Mari, R., and Makse, H. A. (2016). Collective Influence Algorithm to find influencers via optimal percolation in massively large social media. *Scientific reports*, 6:30062.
38. Newman, M. E. and Watts, D. J. (1999). Scaling and percolation in the small-world network model. *Physical Review E - Statistical Physics, Plasmas, Fluids, and Related Interdisciplinary Topics*, 60(6):7332–7342.
39. Newman, M. E. J. (2002). Spread of epidemic disease on networks. *Physical Review E*, 66(1):16128.
40. Ogawa, M., Sone, D., Beheshti, I., Maikusa, N., Okita, K., Takano, H., and Matsuda, H. (2019). Association between subfield volumes of the medial temporal lobe and cognitive assessments. *Heliyon*, 5(6):e01828.
41. Pastor-Satorras, R. and Vespignani, A. (2001). Epidemic spreading in scale-free networks. *Phys. Rev. Lett.*, 86:3200–3203.
42. Piraveenan, M., Prokopenko, M., and Hossain, L. (2013). Percolation Centrality: Quantifying Graph-Theoretic Impact of Nodes during Percolation in Networks. *PLOS ONE*, 8(1):e53095.
43. Reijneveld, J. C., Ponten, S. C., Berendse, H. W., and Stam, C. J. (2007). The application of graph theoretical analysis to complex networks in the brain. *Clinical Neurophysiology*, 118(11):2317–2331.
44. Reuter, M., Schmansky, N. J., Rosas, H. D., and Fischl, B. (2012). Within-subject template estimation for unbiased longitudinal image analysis. *NeuroImage*, 61(4):1402–1418.
45. Richardson, M. and Domingos, P. (2002). Mining knowledge-sharing sites for viral marketing. In *Proceedings of the Eighth ACM SIGKDD International Conference on Knowledge Discovery and Data Mining*, KDD '02, page 61–70, New York, NY, USA. Association for Computing Machinery.

46. Sakkalis, V. (2014). *Modern electroencephalographic assessment techniques: Theory and applications*.
47. Sanchez-Romero, R. and Cole, M. W. (2020). Combining multiple functional connectivity methods to improve causal inferences. *bioRxiv*.
48. Sander, L. M., Warren, C. P., Sokolov, I. M., Simon, C., and Koopman, J. (2002). Percolation on heterogeneous networks as a model for epidemics. *Mathematical biosciences*, 180:293–305.
49. Shaw, L. M., Arias, J., Blennow, K., Galasko, D., Molinuevo, J. L., Salloway, S., Schindler, S., Carrillo, M. C., Hendrix, J. A., Ross, A., Illes, J., Ramus, C., and Fifer, S. (2018). Appropriate use criteria for lumbar puncture and cerebrospinal fluid testing in the diagnosis of Alzheimer's disease. *Alzheimer's & dementia : the journal of the Alzheimer's Association*, 14(11):1505–1521.
50. Son, S. J., Kim, J., Seo, J., min Lee, J., and Park, H. (2015). Connectivity analysis of normal and mild cognitive impairment patients based on FDG and PiB-PET images. *Neuroscience Research*, 98:50–58.
51. Sperling, R. A., Aisen, P. S., Beckett, L. A., Bennett, D. A., Craft, S., Fagan, A. M., Iwatsubo, T., Jack, C. R. J., Kaye, J., Montine, T. J., Park, D. C., Reiman, E. M., Rowe, C. C., Siemers, E., Stern, Y., Yaffe, K., Carrillo, M. C., Thies, B., Morrison-Bogorad, M., Wagster, M. V., and Phelps, C. H. (2011). Toward defining the preclinical stages of Alzheimer's disease: recommendations from the National Institute on Aging-Alzheimer's Association workgroups on diagnostic guidelines for Alzheimer's disease. *Alzheimer's & dementia : the journal of the Alzheimer's Association*, 7(3):280–292.
52. Stam, C. J. and Reijneveld, J. C. (2007). Graph theoretical analysis of complex networks in the brain.
53. Su, Y., Flores, S., Wang, G., Hornbeck, R. C., Speidel, B., Joseph-Mathurin, N., Vlassenko, A. G., Gordon, B. A., Koeppe, R. A., Klunk, W. E., Jack Jr., C. R., Farlow, M. R., Salloway, S., Snider, B. J., Berman, S. B., Roberson, E. D., Brosch, J., Jimenez-Velazques, I., van Dyck, C. H., Galasko, D., Yuan, S. H., Jayadev, S., Honig, L. S., Gauthier, S., Hsiung, G.-Y. R., Masellis, M., Brooks, W. S., Fulham, M., Clarnette, R., Masters, C. L., Wallon, D., Hannequin, D., Dubois, B., Pariente, J., Sanchez-Valle, R., Mummery, C., Ringman, J. M., Bottlaender, M., Klein, G., Milosavljevic-Ristic, S., McDade, E., Xiong, C., Morris, J. C., Bateman, R. J., and Benzinger, T. L. (2019). Comparison of pittsburgh compound b and florbetapir in cross-sectional and longitudinal studies. *Alzheimer's & Dementia: Diagnosis, Assessment & Disease Monitoring*, 11(1):180–190.
54. Tange, O. (2020). Gnu parallel 20200722 ('privacy shield'). GNU Parallel is a general parallelizer to run multiple serial command line programs in parallel without changing them.
55. Tijms, B. M., Wink, A. M., de Haan, W., van der Flier, W. M., Stam, C. J., Scheltens, P., and Barkhof, F. (2013). Alzheimer's disease: connecting findings from graph theoretical studies of brain networks. *Neurobiology of Aging*, 34(8):2023–2036.
56. Tombaugh, T. N., McDowell, I., Kristjansson, B., and Hubley, A. M. (1996). Mini-Mental State Examination (MMSE) and the Modified MMSE (3MS): A psychometric comparison and normative data. *Psychological Assessment*, 8(1):48–59.
57. Vecchio, F., Miraglia, F., and Maria Rossini, P. (2017). Connectome: Graph theory application in functional brain network architecture. *Clinical Neurophysiology Practice*, 2:206–213.
58. Vizza, P., Tradigo, G., Messina, D., Cascini, G. L., and Veltri, P. (2013). Methodologies for the analysis and classification of PET neuroimages. *Network Modeling Analysis in Health Informatics and Bioinformatics*, 2(4):191–208.
59. Wink, A. M. (2019). Eigenvector centrality dynamics from resting-state fmri: Gender and age differences in healthy subjects. *Frontiers in Neuroscience*, 13:648.
60. Wink, A. M., Tijms, B. M., ten Kate, M., Raspor, E., de Munck, J. C., Altena, E., Ecay-Torres, M., Clerigue, M., Estanga, A., Garcia-Sebastian, M., Izagirre, A., Martinez-Lage Alvarez, P., Villanua, J., Barkhof, F., and Sanz-Arigita, E. (2018). Functional brain network centrality is related to apoe genotype in cognitively normal elderly. *Brain and Behavior*, 8(9):e01080.
61. Wook Yoo, S., Han, C. E., Shin, J. S., Won Seo, S., Na, D. L., Kaiser, M., Jeong, Y., and Seong, J. K. (2015). A network flow-based analysis of cognitive reserve in normal ageing and Alzheimer's disease. *Scientific Reports*, 5:1–14.
62. Yamin, G. and Teplow, D. B. (2017). Pittsburgh Compound-B (PiB) binds amyloid β-protein protofibrils. *Journal of neurochemistry*, 140(2):210–215.

8 Supplementary Information

The percolation centrality value is calculated for each network using the inbuilt function of Networkx. This has a worst-case time complexity of $O(n^3)$, where n is the number of nodes in the network. Using a modified form of Brandes' fast algorithm for betweenness centrality, the complexity can be reduced to O(nm), where m is the number of edges. However, percolation centrality calculation with target nodes cannot take advantage of this optimization and has a worst-case time complexity of $O(n^3)$ (see supplementary data)

Table 8 Multivariate Linear Regression Analysis- Region of Interest Across Clinical Conditions for Both Threshold Schemes for Current Flow Betweenness Centrality

	Clinical Condition		CN		MCI		AD	
Graph Metric	PT	Tracer	OMST	SPT	OMST	SPT	OMST	SPT
Current Flow Betweenness Centrality	MMSE	AV45	3	0	1	0	0	0
		PiB	0	0	1	0	0	0
	NPI-Q	AV45	0	0	0	0	0	0
		PiB	0	0	0	0	0	0

Table 9 Multivariate Linear Regression Analysis- Region of Interest Across Clinical Conditions for Both Threshold Schemes for Eigenvector Centrality

	Clinical Condition		CN		MCI		AD	
Graph Metric	PT	Tracer	OMST	SPT	OMST	SPT	OMST	SPT
Eigenvector Centrality	MMSE	AV45	2	2	11	4	7	10
		PiB	2	2	6	6	8	3
	NPI-Q	AV45	1	4	1	1	0	0
		PiB	3	0	3	3	2	9

Table 10 Multivariate Linear Regression Analysis- Region of Interest Across Clinical Conditions for Both Threshold Schemes for Closeness Centrality

	Clinical Condition		CN		MCI		AD	
Graph Metric	PT	Tracer	OMST	SPT	OMST	SPT	OMST	SPT
Closeness Centrality	MMSE	AV45	0	5	1	2	2	1
		PiB	2	4	46	0	6	0
	NPI-Q	AV45	1	0	0	2	0	0
		PiB	3	30	1	0	0	10

PT: Psychometric Assessment, OMST: Orthogonal Minimum Spanning Tree, SPT: Shortest Path Threshold, MMSE: Mini Mental State Examination, NPIQ: Neuropsychiatric Inventory Questionnaire Questionnaire

Table 11 AV45 Betweenness Centrality MMSE Clinical conditions

	CN			MCI			AD		
	ROI	**MMSE Corr**	**MMSE p value**	**ROI**	**MMSE Corr**	**MMSE p value**	**ROI**	**MMSE Corr**	**MMSE p value**
OMST	GM Visual cortex V1 BA17 R	-0.38971	0.00001	GM Visual cortex V2 BA18 R	-0.34972	0.00170	GM Superior parietal lobule 7A R	-0.49356	0.02700
	GM Secondary somatosensory cortex / Parietal operculum OP3 R	-0.21594	0.01937	GM Hippocampus subiculum L	-0.28648	0.01100	WM Fornix	0.46021	0.04117
	GM Hippocampus hippocampal-amygdaloid transition area R	-0.19910	0.03139	WM Superior longitudinal fascicle R	-0.27073	0.01651	GM Primary somatosensory cortex BA2 R	0.47950	0.03241
	GM Insula Ig1 L	-0.18830	0.04204	GM Secondary somatosensory cortex / Parietal operculum OP1 R	-0.26697	0.01814	GM Visual cortex V2 BA18 L	0.56184	0.00993
				GM Visual cortex V2 BA18 L	-0.24971	0.02747			
				WM Cingulum R	-0.24874	0.02809			
				GM Inferior parietal lobule PFm R	-0.24212	0.03270			
				GM Anterior intra-parietal sulcus hIP1 R	-0.24114	0.03344			
				GM Superior parietal lobule 7P R	-0.23361	0.03955			
				GM Lateral geniculate body R	-0.23251	0.04051			
				GM Hippocampus cornu ammonis R	-0.23043	0.04239			
				GM Primary somatosensory cortex BA3b L	-0.22411	0.04855			
				GM Primary somatosensory cortex BA3b R	-0.22340	0.04928			
SP	GM Secondary somatosensory cortex / Parietal operculum OP1 L	-0.26168	0.00437	GM Primary somatosensory cortex BA3a R	-0.31886	0.00444	GM Superior parietal lobule 5Ci L	-0.58485	0.00676
	WM Optic radiation L	-0.25794	0.00499	GM Visual cortex V3V L	-0.31700	0.00469	GM Superior parietal lobule 7A L	-0.58218	0.00708
	GM Superior parietal lobule 7PC L	-0.23427	0.01101	GM Hippocampus dentate gyrus L	-0.30085	0.00744	GM Superior parietal lobule 7P L	-0.46195	0.04031
	GM Secondary somatosensory cortex / Parietal operculum OP4 R	-0.19851	0.03190	GM Superior parietal lobule 7PC L	-0.24379	0.03149	WM Cingulum L	-0.45827	0.04214
	GM Primary somatosensory cortex BA3a L	-0.19065	0.03950	GM Anterior intra-parietal sulcus hIP3 L	-0.22437	0.04829	GM Inferior parietal lobule PFcm R	-0.44748	0.04789
				GM Primary somatosensory cortex BA3b L	-0.22273	0.04999	WM Superior longitudinal fascicle L	0.48106	0.03177
				WM Superior occipito-frontal fascicle L	0.28715	0.01080	GM Primary somatosensory cortex BA3b R	0.49437	0.02671
				GM Premotor cortex BA6 L	0.29446	0.00887			

Table 12 AV45 Percolation Centrality MMSE Clinical conditions

	CN			MCI			AD		
	ROI	**MMSE Corr**	**MMSE p value**	**ROI**	**MMSE Corr**	**MMSE p value**	**ROI**	**MMSE Corr**	**MMSE p value**
OMST	GM Visual cortex V1 BA17 R	-0.3953	0.0000	GM Visual cortex V2 BA18 R	-0.3323	0.0030	GM Superior parietal lobule 7A R	-0.4886	0.0288
	GM Secondary somatosensory cortex / Parietal operculum OP3 R	-0.2128	0.0212	GM Hippocampus subiculum L	-0.2917	0.0096	WM Fornix	0.4601	0.0412
	GM Hippocampus hippocampal-amygdaloid transition area R	-0.1969	0.0334	GM Secondary somatosensory cortex / Parietal operculum OP1 R	-0.2686	0.0174	GM Primary somatosensory cortex BA2 R	0.4803	0.0321
	GM Insula Ig1 L	-0.1875	0.0430	WM Superior longitudinal fascicle R	-0.2680	0.0177	GM Visual cortex V2 BA18 L	0.5631	0.0097
				GM Anterior intra-parietal sulcus hIP1 R	-0.2546	0.0245			
				GM Visual cortex V2 BA18 L	-0.2534	0.0252			
				WM Cingulum R	-0.2443	0.0311			
				GM Inferior parietal lobule PFm R	-0.2407	0.0337			
				GM Superior parietal lobule 7P R	-0.2329	0.0402			
				GM Hippocampus cornu ammonis R	-0.2282	0.0445			
				GM Lateral geniculate body R	-0.2261	0.0465			
				GM Primary somatosensory cortex BA3b L	-0.2230	0.0497			
SP	GM Secondary somatosensory cortex / Parietal operculum OP1 L	-0.2594	0.0047	WM Superior occipito-frontal fascicle L	0.2856	0.0113	GM Superior parietal lobule 5Ci L	-0.5892	0.0063
	WM Optic radiation L	-0.2558	0.0054	GM Premotor cortex BA6 L	0.2921	0.0095	GM Superior parietal lobule 7A L	-0.5877	0.0064
	GM Superior parietal lobule 7PC L	-0.2431	0.0083				GM Superior parietal lobule 7P L	-0.4685	0.0372
	GM Secondary somatosensory cortex / Parietal operculum OP4 R	-0.1985	0.0320				WM Cingulum L	-0.4570	0.0428
	GM Primary somatosensory cortex BA3a L	-0.1867	0.0438				GM Inferior parietal lobule PFcm R	-0.4473	0.0480
	WM Superior longitudinal fascicle R	-0.1817	0.0499				WM Superior longitudinal fascicle L	0.4766	0.0336
							GM Primary somatosensory cortex BA3b R	0.4964	0.0260

Table 13 PiB Betweenness Centrality MMSE Clinical conditions

	CN			MCI			AD		
	ROI	**MMSE Corr**	**MMSE p value**	**ROI**	**MMSE Corr**	**MMSE p value**	**ROI**	**MMSE Corr**	**MMSE p value**
OMST	GM Primary auditory cortex TE1.2 R	0.5860	0.0353	GM Secondary somatosensory cortex / Parietal operculum OP4 L	-0.3357	0.0093	GM Inferior parietal lobule Pga L	-0.5288	0.0291
	GM Superior parietal lobule 7P R	0.6021	0.0294	GM Superior parietal lobule 5L L	-0.3279	0.0112	GM Inferior parietal lobule PFm L	-0.4905	0.0456
	WM Fornix	0.6489	0.0164	GM Primary somatosensory cortex BA3b L	-0.2904	0.0256			
	GM Secondary somatosensory cortex / Parietal operculum OP2 R	0.6647	0.0132	GM Primary somatosensory cortex BA2 L	-0.2867	0.0277			
	WM Superior longitudinal fascicle R	0.6695	0.0123	GM Broca's area BA44 R	0.2630	0.0442			
SP	GM Secondary somatosensory cortex / Parietal operculum OP2 L	-0.6944	0.0084	WM Superior longitudinal fascicle R	0.2571	0.0493	GM Inferior parietal lobule PFm L	-0.5995	0.0110
	GM Visual cortex V5 L	-0.5542	0.0494				GM Visual cortex V4 R	-0.5763	0.0155
	GM Inferior parietal lobule PF L	0.6385	0.0188				GM Visual cortex V2 BA18 R	-0.5448	0.0237
	GM Inferior parietal lobule PFt L	0.7274	0.0048				GM Secondary somatosensory cortex / Parietal operculum OP1 L	-0.5441	0.0240
							GM Visual cortex V1 BA17 L	-0.5144	0.0346
							GM Inferior parietal lobule Pga L	-0.4966	0.0426
							GM Superior parietal lobule 7M L	-0.4964	0.0427
							GM Anterior intra-parietal sulcus hIP3 L	-0.4875	0.0471
							GM Hippocampus entorhinal cortex L	-0.4838	0.0491

Table 14 PiB Percolation Centrality MMSE Clinical conditions

	CN			MCI			AD		
	ROI	**MMSE Corr**	**MMSE p value**	**ROI**	**MMSE Corr**	**MMSE p value**	**ROI**	**MMSE Corr**	**MMSE p value**
OMST	GM Primary auditory cortex TE1.2 R	0.59077	0.03350	GM Secondary somatosensory cortex / Parietal operculum OP4 L	-0.33750	0.00895	GM Inferior parietal lobule Pga L	-0.51018	0.03641
	GM Superior parietal lobule 7P R	0.60439	0.02868	GM Superior parietal lobule 5L L	-0.33027	0.01063	GM Inferior parietal lobule PFm L	-0.49655	0.04261
	WM Fornix	0.64905	0.01638	GM Primary somatosensory cortex BA3b L	-0.29131	0.02519			
	GM Secondary somatosensory cortex / Parietal operculum OP2 R	0.66156	0.01379	GM Primary somatosensory cortex BA2 L	-0.28578	0.02823			
	WM Superior longitudinal fascicle R	0.66684	0.01279	GM Broca's area BA44 R	0.26177	0.04521			
SP	GM Secondary somatosensory cortex / Parietal operculum OP2 L	-0.70639	0.00696				GM Inferior parietal lobule PFm L	-0.60706	0.00976
	GM Inferior parietal lobule PF L	0.63646	0.01934				GM Visual cortex V4 R	-0.58416	0.01380
	GM Inferior parietal lobule PFt L	0.72476	0.00507				GM Secondary somatosensory cortex / Parietal operculum OP1 L	-0.55953	0.01952
							GM Visual cortex V2 BA18 R	-0.54932	0.02237
							GM Visual cortex V1 BA17 L	-0.53297	0.02760
							GM Hippocampus entorhinal cortex L	-0.49221	0.04474
							GM Anterior intra-parietal sulcus hIP3 L	-0.48753	0.04713
							GM Superior parietal lobule 7M L	-0.48449	0.04874
							GM Inferior parietal lobule Pga L	-0.48399	0.04900

Table 15 AV45 Betweenness Centrality NPIQ Clinical conditions

	CN			MCI			AD		
	ROI	**NPIQ Corr**	**NPIQ p value**	**ROI**	**NPIQ Corr**	**NPIQ p value**	**ROI**	**NPIQ Corr**	**NPIQ p value**
OMST				GM Secondary somatosensory cortex / Parietal operculum OP4 R	-0.38395	0.03005			
SP	GM Inferior parietal lobule PGp R	0.56843	0.02704	GM Hippocampus hippocampal-amygdaloid transition area R	0.40439	0.02170	GM Superior parietal lobule 5Ci L	-0.58485	0.00676
	WM Optic radiation R	0.58201	0.02283				GM Superior parietal lobule 7A L	-0.58218	0.00708
	GM Secondary somatosensory cortex / Parietal operculum OP3 L	0.82598	0.00015				GM Superior parietal lobule 7P L	-0.46195	0.04031
							WM Cingulum L	-0.45827	0.04214
							GM Inferior parietal lobule PFcm R	-0.44748	0.04789
							WM Superior longitudinal fascicle L	0.48106	0.03177
							GM Primary somatosensory cortex BA3b R	0.49437	0.02671

Table 16 AV45 Percolation Centrality NPIQ Clinical conditions

	CN			MCI			AD		
	ROI	**NPIQ Corr**	**NPIQ p value**	**ROI**	**NPIQ Corr**	**NPIQ p value**	**ROI**	**NPIQ Corr**	**NPIQ p value**
OMST	GM Inferior parietal lobule PFcm R	0.51951	0.04717	GM Secondary somatosensory cortex / Parietal operculum OP4 R	-0.37988	0.03199			
	GM Hippocampus hippocampal-amygdaloid transition area R	0.57396	0.02526	GM Inferior parietal lobule PFcm R	-0.35247	0.04787			
	GM Secondary somatosensory cortex / Parietal operculum OP4 R	0.61824	0.01403						
	GM Inferior parietal lobule PFop R	0.62373	0.01296						
	GM Medial geniculate body L	0.66804	0.00649						
	GM Primary auditory cortex TE1.0 R	0.67251	0.00602						
SP	WM Optic radiation R	0.55752	0.03082	GM Hippocampus hippocampal-amygdaloid transition area R	0.41665	0.01768			
	GM Inferior parietal lobule PGp R	0.57839	0.02390						
	GM Secondary somatosensory cortex / Parietal operculum OP3 L	0.83786	0.00010						

Table 17 PiB Betweenness Centrality NPIQ Clinical conditions

	CN			MCI			AD		
	ROI	**NPIQ Corr**	**NPIQ p value**	**ROI**	**NPIQ Corr**	**NPIQ p value**	**ROI**	**NPIQ Corr**	**NPIQ p value**
OMST	WM Uncinate fascicle R	0.57017	0.04189	GM Inferior parietal lobule PF R	0.24701	0.04730	GM Inferior parietal lobule PFop L	0.49369	0.03170
	GM Amygdala_superficial group R	0.88598	0.00006				GM Secondary somatosensory cortex / Parietal operculum OP4 L	0.51946	0.02265
							GM Inferior parietal lobule PFm L	0.72371	0.00046
SP	GM Medial geniculate body R	0.60961	0.02697	GM Inferior parietal lobule PF R	0.24701	0.04730	GM Insula Id1 R	0.46020	0.04741
	GM Inferior parietal lobule PFt L	0.61877	0.02415				GM Primary auditory cortex TE1.2 L	0.51224	0.02494
	GM Premotor cortex BA6 R	0.65567	0.01497				WM Acoustic radiation L	0.51903	0.02278
	GM Broca's area BA44 L	0.68292	0.01009				GM Insula Ig2 L	0.52267	0.02168
	GM Inferior parietal lobule PFop R	0.68571	0.00967				GM Medial geniculate body L	0.55444	0.01376
	GM Inferior parietal lobule PFcm R	0.69232	0.00873				GM Inferior parietal lobule PF L	0.56824	0.01114
	GM Hippocampus hippocampal-amygdaloid transition area R	0.70249	0.00742				GM Primary auditory cortex TE1.0 L	0.59007	0.00783
	GM Insula Id1 R	0.74143	0.00372				GM Amygdala_centromedial group R	0.62051	0.00459
	GM Amygdala_centromedial group L	0.74174	0.00370				GM Inferior parietal lobule PFm R	0.66918	0.00173
	GM Secondary somatosensory cortex / Parietal operculum OP3 L	0.79122	0.00127				GM Inferior parietal lobule PGp L	0.72702	0.00042
	GM Secondary somatosensory cortex / Parietal operculum OP1 L	0.80353	0.00094						
	GM Inferior parietal lobule Pga R	0.80529	0.00089						
	GM Amygdala_superficial group L	0.80656	0.00086						
	GM Inferior parietal lobule PF R	0.81603	0.00067						

Table 18 PiB Percolation Centrality NPIQ Clinical conditions

	CN			MCI			AD		
	ROI	**NPIQ Corr**	**NPIQ p value**	**ROI**	**NPIQ Corr**	**NPIQ p value**	**ROI**	**NPIQ Corr**	**NPIQ p value**
OMST	WM Uncinate fascicle R	0.56123	0.04597	GM Inferior parietal lobule PF R	0.25158	0.04322	GM Inferior parietal lobule PFop L	0.48286	0.03625
	GM Amygdala_superficial group R	0.88441	0.00006				GM Secondary somatosensory cortex / Parietal operculum OP4 L	0.52807	0.02013
							GM Inferior parietal lobule PFm L	0.71099	0.00064
SP	GM Medial geniculate body R	0.60951	0.02700	GM Inferior parietal lobule PFm R	0.25558	0.03990	GM Insula Id1 R	0.46747	0.04358
	GM Inferior parietal lobule PFt L	0.61126	0.02644				GM Primary auditory cortex TE1.2 L	0.50560	0.02722
	GM Insula Id1 R	0.65621	0.01486				GM Insula Ig2 L	0.50874	0.02612
	GM Premotor cortex BA6 R	0.65838	0.01442				WM Acoustic radiation L	0.52368	0.02138
	GM Inferior parietal lobule PFcm R	0.67041	0.01215				GM Medial geniculate body L	0.54919	0.01487
	GM Broca's area BA44 L	0.68677	0.00952				GM Inferior parietal lobule PF L	0.57114	0.01064
	GM Inferior parietal lobule PFop R	0.69406	0.00849				GM Primary auditory cortex TE1.0 L	0.58632	0.00833
	GM Hippocampus hippocampal-amygdaloid transition area R	0.70205	0.00747				GM Amygdala_centromedial group R	0.63041	0.00381
	GM Amygdala_centromedial group L	0.75277	0.00298				GM Inferior parietal lobule PFm R	0.67064	0.00167
	GM Secondary somatosensory cortex / Parietal operculum OP3 L	0.79262	0.00123				GM Inferior parietal lobule PGp L	0.72603	0.00043
	GM Secondary somatosensory cortex / Parietal operculum OP1 L	0.80452	0.00091						
	GM Inferior parietal lobule Pga R	0.80559	0.00089						
	GM Amygdala_superficial group L	0.80656	0.00086						
	GM Inferior parietal lobule PF R	0.81670	0.00066						